Differentiation of sCJD and vCJD Forms by Automated Analysis of Basal Ganglia Intensity Distribution in Multisequence MRI of the Brain—Definition and Evaluation of New MRI-Based Ratios

Marius George Linguraru*, Nicholas Ayache, Eric Bardinet, Miguel Ángel González Ballester, Damien Galanaud, Stéphane Haïk, Baptiste Faucheux, Jean-Jacques Hauw, Patrick Cozzone, Didier Dormont, and Jean-Philippe Brandel

***Abstract*—We present a method for the analysis of basal ganglia (including the thalamus) for accurate detection of human spongiform encephalopathy in multisequence magnetic resonance imaging (MRI) of the brain. One common feature of most forms of prion protein diseases is the appearance of hyperintensities in the deep grey matter area of the brain in T2-weighted magnetic resonance (MR) images. We employ T1, T2, and Flair-T2 MR sequences for the detection of intensity deviations in the internal nuclei. First, the MR data are registered to a probabilistic atlas and normalized in intensity. Then smoothing is applied with edge enhancement. The segmentation of hyperintensities is performed using a model of the human visual system. For more accurate results, *a priori* anatomical data from a segmented atlas are employed to refine the registration and remove false positives. The results are robust over the patient data and in accordance with the clinical ground truth. Our method further allows the quantification of intensity distributions in basal ganglia. The caudate nuclei are highlighted as main areas of diagnosis of sporadic Creutzfeldt–Jakob Disease (sCJD), in agreement with the histological data. The algorithm permitted the classification of the intensities of abnormal signals in sCJD patient FLAIR images with a higher hypersignal in caudate nuclei (10/10) and putamen (6/10) than in thalami. Defining normalized MRI measures of the intensity relations between the internal grey nuclei of patients, we robustly differentiate sCJD and variant CJD (vCJD) patients, in an attempt to create an automatic classification tool of human spongiform encephalopathies.**

***Index Terms*—Creutzfeldt–Jakob Disease (CJD), grey matter (GM), human visual system model, intensity quantification, internal nuclei, multisequence magnetic resonance imaging (MRI) of the brain, normalization, registration, segmentation, sporadic Creutzfeldt–Jakob Disease (sCJD), variant Creutzfeldt–Jakob Disease (vCJD).**

Manuscript received September 27, 2005; revised March 28, 2006. This work was supported in part by the GIS-Prions project (see the partaking centers under the authors' names) coordinated by J.-P. Brandel. *Asterisk indicates corresponding author.*

*M. G. Linguraru is with the Epidaure/Asclepios Research Group—INRIA, 06902 Sophia Antipolis Cedex, France, and with the Department of Engineering and Applied Sciences, Harvard University, Cambridge, MA 02138 USA (e-mail: mglin@deas.harvard.edu).

N. Ayache is with the Epidaure/Asclepios Research Group—INRIA, 06902 Sophia Antipolis Cedex, France.

E. Bardinet is with the CNRS UPR640-LENA, 75651 Paris, France.

M. Á. González Ballester is with the Epidaure/Asclepios Research Group—INRIA, 06902 Sophia Antipolis Cedex, France, and with the MEM-ISTB, University of Bern, CH-3014 Bern, Switzerland.

D. Galanaud is with the Department of Neuroradiology, La Pitié-Salpêtrière Hospital, 75013 Paris, France, and with the CRMBM UMR CNRS 6612, Faculty of Medicine, 13005 Marseille, France.

S. Haïk is with the INSERM U360, La Pitié-Salpêtrière Hospital, 75651 Paris, France, and with the R. Escourolle Neuropathological Laboratory, La Pitié-Salpêtrière Hospital, 75651 Paris, France, and also with The National Reference Cell of CJD, La Pitié-Salpêtrière Hospital, 75651 Paris, France.

B. Faucheux and J.-J. Hauw are with the INSERM U360, La Pitié-Salpêtrière Hospital, 75651 Paris, France, and with the R. Escourolle Neuropathological Laboratory, La Pitié-Salpêtrière Hospital, 75651 Paris, France.

P. Cozzone is with the CRMBM UMR CNRS 6612, Faculty of Medicine, 13005 Marseille, France.

D. Dormont is with the CNRS UPR640-LENA, 75651 Paris, France, and with the Department of Neuroradiology, La Pitié-Salpêtrière Hospital, 75013 Paris, France.

J.-P. Brandel is with the INSERM U360, La Pitié-Salpêtrière Hospital, 75651 Paris, France, and with the The National Reference Cell of CJD, La Pitié-Salpêtrière Hospital, 75651 Paris, France.

Digital Object Identifier 10.1109/TMI.2006.876133

I. Introduction

THE identification of diagnosis markers is a major challenge in the clinical care of patients with Creutzfeldt–Jakob Disease (CJD). This disease raises a number of questions for neuroradiological centers, due to the limited development of medical imaging techniques for its detection. Some recent studies [5], [15], [22], [52] found strong correspondences between the diagnosis of CJD and the detection of signal abnormality in the deep grey matter (GM) internal nuclei in magnetic resonance imaging (MRI) of the brain. Since CJD progresses rapidly, detecting the earliest signs of the disease becomes essential in studying its evolution and developing potential treatments.

This work was completed as part of GIS-Prions, a project funded by the French Ministry of Health. Its goal was to perform a prospective study of particularly sporadic Creutzfeldt–Jakob disease (sCJD) and variant Creutzfeldt–Jakob disease (vCJD) and develop techniques for the detection and classification of various types of CJD [5], [6]. The project involved several research centers across France and a database aimed at including CJD patients from two main neuroradiological centers in Paris and Marseille in the period between 2002 and 2004. All patients gave their informed written consent. The protocol was reviewed and approved by the local ethical committee (CCPPRB).

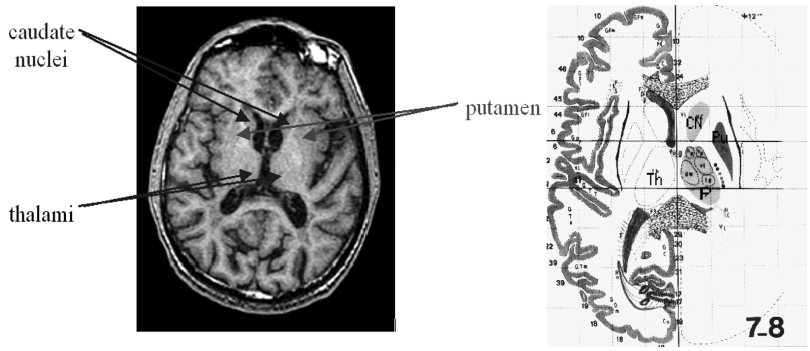

Fig. 1. Deep grey nuclei. On the left: a map of deep GM internal nuclei in a normal T1-weighted axial MR image. On the right: a map of deep GM internal nuclei reproduced from the Talairach and Tournoux atlas [45] showing the caudate nuclei (CN), the putamen (Pu), and the thalami (Th). Pulvinar (P) is located in the posterior section of the thalamus.

A. CJD and MRI

MRI is commonly used for noninvasive examinations of patients with neurological diseases [23], [44]. For the last fifteen years, evidence of MRI hypersignals in CJD patients has been found. However, the observations and studies describing the MRI ability to help in the diagnosis of CJD are in an early stage. Most of the studies are concerned with sCJD cases, which represent 80% of all forms of CJD. The first study cases describe hypersignals in T2-weighted images (and FLAIR T2 images) with higher incidence in the basal ganglia (see Fig. 1) in a bilateral symmetric form [18], [33], [37]. Schroeter *et al.* [41] conduct a large study on sCJD patients and conclude that the MR sensitivity in detecting sCJD is 67% with a specificity of 93%. No anomalies are generally reported in T1-weighted images of sCJD patients, with some exceptions [13].

A great concern has been the occurrence in the U.K. of vCJD in the 1990s, a form of environmentally acquired human CJD. Although the number of vCJD cases has decreased since 2001, there is a new risk of rise by blood transfusion [39]. This type of CJD related to the bovine spongiform encephalopathy shows a different distribution of lesions and therefore hyperintensities in brain MRI [36], [51]. In FLAIR and T2 sequences, abnormal high signals are depicted in the thalamus, mainly in the posterior pulvinar nucleus (see Fig. 1). Unlike in sCJD cases, in vCJD cases abnormal intensities are higher in the pulvinar when compared to striatum [20]. The sensitivity of MRI in detecting vCJD is reported as 78% with a specificity of 100%.

Cortical hypersignals are also associated with CJD, but on a much more reduced scale. Abnormal cortical signals are best detected in diffusion weighted images (DWIs) [3]. Areas of high signal in DWI are usually associated with decreased apparent diffusion coefficient (ADC) values [24], [43]. Although there are overlaps between bright areas in FLAIR/T2 and in DWI, the MR sequences depict different types of abnormal pathological features.

There are several hypotheses relating hyperintensities in MRI and CJD. In [14] and [46], the interpretation of MRI studies and neuropathological data shows that an elevation of signal in MRI T2-weighted sequences correlates with gliosis in pathological analysis. Bahn and Parchi [4] relate the high signal in DWI to spongiform changes. In [51] and [52], it is argued that hyperintensities in thalamus in vCJD seem more likely linked to the level of gliosis than to spongiosis or prion deposits. More recently, Haïk *et al.* [21] noted that in a sCJD and vCJD cases, there is no clear association between the high MRI signal and gliosis or spongiform changes. It seems to be closer related to the accumulation of prion protein. Still, the relation between the prion deposits and strong signal in MRI remains ambiguous.

Some studies make MR related image processing an important tool in noninvasive CJD diagnosis [17], [33], [35]. However, the visual interpretation of MR images by the clinicians is sometimes difficult and could lead to an under- or overestimation of the true incidence of CJD [6]. At the present time, MRI is not included as a diagnosis criterion for sCJD, even though it could be useful, as for vCJD [52]. Therefore, it is necessary to further explore the advantages of computer aided diagnosis (CAD) techniques in the MRI clinical environment.

Leemput [46] proposes a method for automated quantification of MR intensity changes in images of CJD patients. He acknowledges common difficulties in processing such images, including limited resolution, partial volume effects, noise, low contrast, and nonhomogeneous intensity, whether a computer or a human expert performs it. Hence, low-level segmentation methods are inappropriate for the detection of hyperintensities in the affected areas of the brain. A mixture model of normal distributions combined with the expectation-maximisation algorithm (EM) is proposed. However, the method does not detect signal abnormalities in all the CJD cases, while showing significant amounts of false positives (FPs) along the interface between GM and cerebrospinal fluid (CSF).

Colchester, Hojjat *et al.* [9], [10], [22] analyse the putamen intensity gradient to separate CJD from normals and propose several ratios (posterior thalamus to caudate and most notably to frontal white matter) to differentiate vCJD from the rest. They use T2-weighted and proton density MRI for average intensities (no hyperintensity analysis) and their segmentation is performed manually.

B. Addressing the Problem

CAD is expected to simplify the complex tasks of every day clinical work, assist in the routine investigation of large numbers of medical images (reducing human errors), and present a robust and reliable second opinion in decision making.

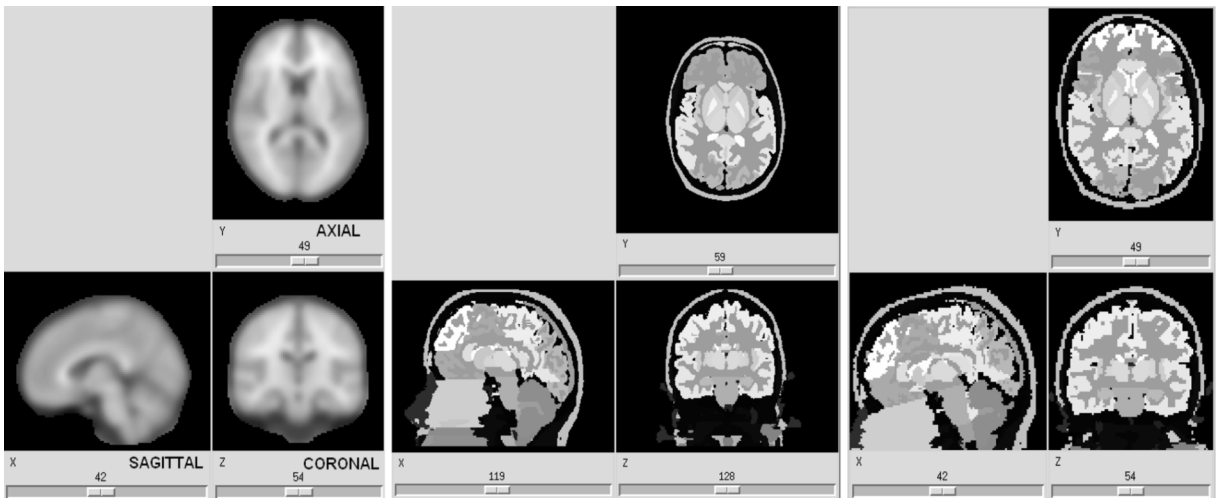

Fig. 2. Registration of Zubal Phantom onto the MNI template. On the left, the MNI template; in the middle, the original Zubal Phantom; the right image shows the registered Zubal Phantom. Please note the arrangement of MR images in radiological convention with an axial, a sagittal and a coronal view. This convention is reflected in figures throughout the paper.

The image blurring due to motion artefacts in the set of images we work with makes the use of statistical detection algorithms very difficult. Such algorithms rely on finding consistent repeatable signs of a disease over a set of patients [26], [48]. Also, they need good contrast between GM and white matter (WM) in T1-weighted images for stochastic analysis according to a general atlas context. This is another major source of errors in cases of CJD, where patients suffer dementia with often uncontrolled movements.

Rueckert *et al.* [40] build statistical deformation models of anatomical variability. They use nonrigid registration to build atlases of the brain and patient anatomical models. Since we use images with low contrast, our method combines affine and nonrigid registration using global landmarks to segment deep grey nuclei.

The approach we propose is based on the use of *a priori* anatomical knowledge in the form of an accurately segmented and labelled image (e.g., the Zubal Phantom [53]) for precise segmentation and of a probabilistic atlas for intra- and interpatient analysis. A feature detection technique based on a model of the human visual system (HVS) is employed for the depiction of hypersignals. We differentiate different types of human prion diseases (sCJD from vCJD) based on the lesions' topographical distribution. The remainder of this paper is organized as follows.

- Section II presents the steps employed on images before the effective segmentation of abnormal intensities. They include spatial and intensity normalization, atlas alignment, and noise removal.
- Section III introduces the refined registration of internal nuclei using a labelled atlas. Then we present the HVS-based detector, an adaptive thresholding method that follows the function of the human eye to segment abnormalities in deep GM. We further define MRI-based ratios for the prompting and differentiation of CJD forms.
- Results of our method to detect and quantify intensity distributions in deep grey nuclei are illustrated in Section IV.

II. Preprocessing

In this section, we review the preprocessing stages used before the actual segmentation of CJD hypersignals. This is a model of data normalization and regularisation, which is required to put the images in the same general framework to reduce the number of parameters.

The image acquisition protocol is designed to include three MRI sequences for each patient. The sequences used by our algorithm are: a T1-weighted acquisition for its higher contrast between GM and WM and higher image resolution; T2-weighted images for its strong contrast between CSF and brain parenchyma; and a T2-weighted FLAIR sequence for the depiction of CJD signs in the brain.

A. Image Normalization

The large variability inherent to human anatomy and imaging parameters leads us to consider spatial and intensity normalization as an approach to normalize patient images for further abnormality detection. This is done both to localize the areas of interest with the help of an atlas of the brain, and to normalize specific imaging parameters for an automatic detection of the affected brain areas. Furthermore, interpatient analysis could now be performed.

1) Spatial Normalization: Data registration to an atlas has become a common technique with the introduction of popular statistical algorithms for image processing, such as statistical parametric mapping (SPM) [2] or expectation maximization segmentation (EMS) [48]. A well-known probabilistic atlas in the scientific community is the MNI Atlas from the Montreal Neurological Institute at McGill University [11]. Built using over 300 MRI scans of healthy individuals to compute an average brain MR image, the MNI template is now the standard template of SPM and the International Consortium for Brain Mapping [32] (see Fig. 2 left).

We propose the following registration scheme. T1 images have the highest resolution in our data set; hence, we register

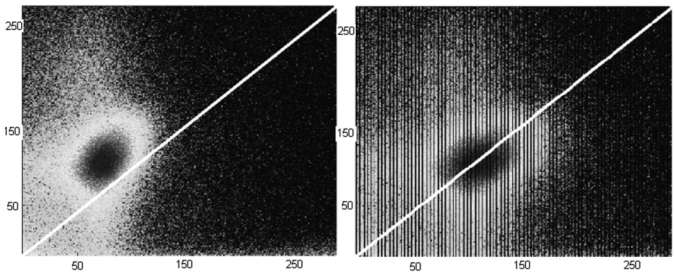

Fig. 3. Joint histograms of the two MR patient images before intensity normalization (left) and after the affine regularisation of intensities (right). Note the realignment of the cloud of points in the middle of images to fit better the first diagonal (shown in white) once the image normalization has been performed. Dark vertical lines appearing in the histogram of normalized images are caused by the dilation of the range of intensities in the image to be normalized; as we work with discrete data and we do not employ any interpolation, the affine normalization will not cover the entire range between the minimum and maximum values.

them to the MNI template using an affine transformation. The registration algorithm, previously developed in our group, is described in [37]. It uses a block matching strategy at multiple scales assuming that there is a global intensity relationship between the template image and the one being registered to it. Next, rigid intra-patient registration of the T2 and the FLAIR sequences to the T1 image is performed. By combining this rigid transformation with the affine transformation matching the T1 and the MNI template, we can find correspondences between the T2 and FLAIR patient images and the atlas. The final image resolution is that of the MNI atlas: $91 \times 109 \times 91$ voxels.

2) Intensity Normalization: In addition to geometric variability, MR images may also exhibit intensity differences. Common problems in image analysis arise from the considerable variations between images of different patients, but also in images of the same patient taken at different times. As a result, it is difficult to tune processing parameters for good repeatable results. We propose the use of an intensity normalization algorithm for the FLAIR images, prior to the detection of signal deviations. Our method performs an affine equalisation using the joint histogram of two images: a standard image (from our database) onto which we align the intensity distribution of the second image [27].

The two images must be registered prior to normalization in intensity. Ideally, the joint histogram will be as close as possible to a straight line along the first diagonal of the intensity plane. In practice, a joint histogram between MR images of different subjects following the same acquisition protocol resembles a cloud of points centred on a line ($I_2 = aI_1 + b$) in the intensity surface. The affine equalisation we employ finds the parameters a and b by minimizing the criterion C in (1), where i relates to the points of coordinates (I_{1i}, I_{2i}) in the joint histogram. The orthogonal distance is preferred to the vertical distance, which is biased toward one of the two images to align in intensity. Note the change in the joint histogram of two MR images before and after intensity normalization in Fig. 3. This intensity normalization process takes place on images after affine registration to the MNI atlas. Although this registration is not perfect and, as described in following sections, nonrigid registration is required to obtain alignment of fine details, the computation of this global intensity transformation is fairly robust to small misalignments, as it is computed from the histogram of the whole image. Furthermore, the aim is to scale the histograms to fall within the same range of intensities without affecting image contrast, which is the key feature for further segmentation

$$C = \sum_i \frac{|I_{2i} - (aI_{1i} + b)|^2}{a^2 + 1}. \tag{1}$$

B. Noise Removal and Image Enhancement

MR images are noisy. Our application aims to detect areas of abnormal intensity in the deep GM of the brain and noise can hamper the segmentation process. Thus, we smooth our images, but ensure that the areas of interest (areas of high intensity) are preserved for accurate segmentation. We employ an anisotropic diffusion filter based on the diffusion tensor introduced by Weickert [49].

The choice of related eigenvalues (λ) determines the behaviour of the feature detector, as in (2), where I is the image to diffuse. We employ a strong decreasing diffusivity-like function (see power 12) that encourages the fast removal of small noise, while contrast at edges is enhanced. Empirically, the choice of a small contrast threshold $(k = 1)$ gave repeated good results with respect to noise smoothing without influencing the segmentation of hyperintensities. Since the subsequent intensity quantification is based on MR values before smoothing or normalising in intensity, this latter process is not sensitive to the diffusion filter and its parameters. An example of image diffusion is presented in Fig. 4

$$\lambda = \begin{cases} 1 & |\nabla I_\sigma| = 0 \\ 1 - \exp\left(\frac{-1}{(|\nabla I_\sigma|/k)^{12}}\right) & |\nabla I_\sigma| > 0 \end{cases}. \tag{2}$$

III. Segmentation and Intensity Quantification

Our analysis is based on the abnormal MR intensities that can appear in the basal ganglia (including the thalamus) of CJD patients, which often show signs of dementia. Under the given circumstances, the segmentation of GM (where CJD affections are visible) cannot be done directly from the patient images, due to patient movement and therefore low contrast in images. The MNI atlas can provide a probabilistic segmentation of GM, but this is not precise enough for our application. We use instead a segmented anatomical atlas of the brain, the Zubal Phantom [53], which is introduced in the next section.

A. A Priori Anatomical Data

The data we use were affinely registered to the MNI atlas. While we avoid direct nonrigid registration to the MNI atlas, which is an averaged image and lacks detail, the affine registration is only approximate. A precise local intensity analysis of internal nuclei would be erroneous at this stage and, therefore, a

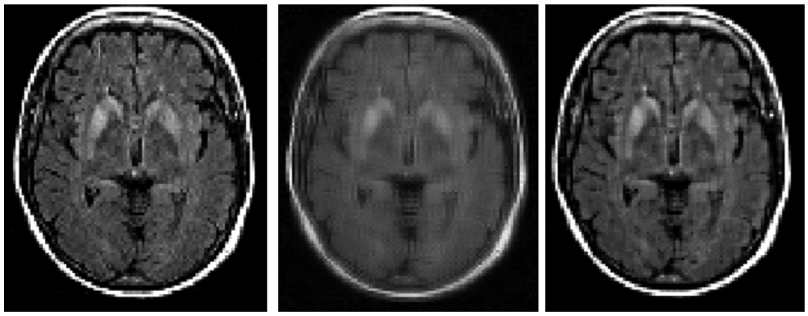

Fig. 4. Effect of anisotropic versus linear diffusion on image smoothing. On the left, we show the original image from a patient with CJD hypersignals in the basal ganglia. In the middle, the linearly diffused (Gaussian convolution) image after five iterations. On the right, the anisotropically diffused image after five iterations with smooth areas and well-preserved edges.

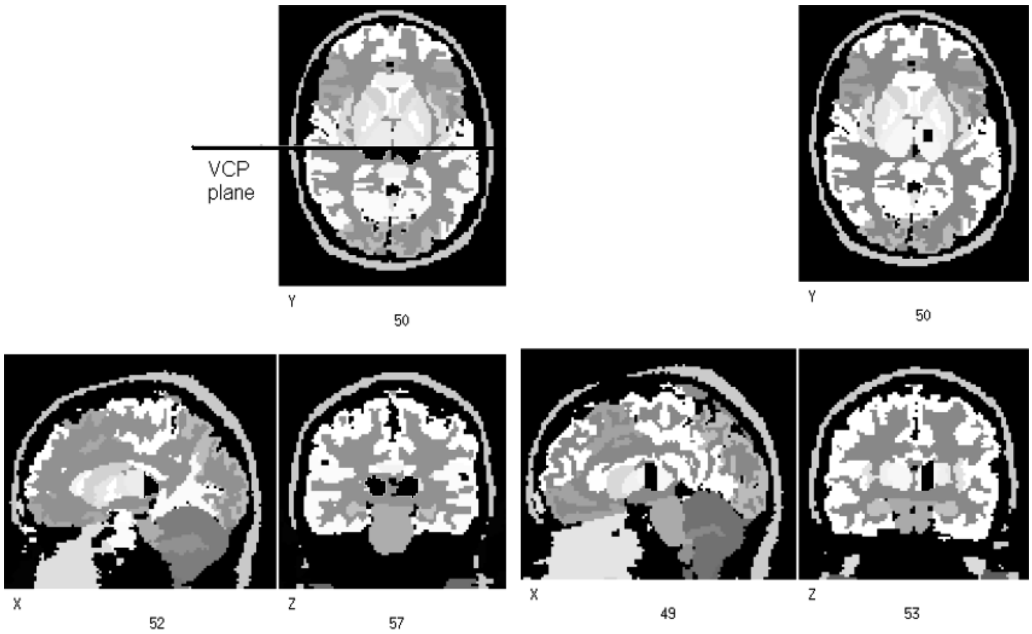

Fig. 5. Definition of pulvinar and anterior thalami in the Zubal Phantom. On the left, the pulvinar is highlighted in black as the thalamic area below the VCP plane. On the right, the "anterior thalamus" is shown in black, a depicted region in the "healthy" area of thalamus.

registration refinement becomes necessary. The Zubal atlas offers a precisely labelled segmentation of brain structures from the T1-weighted MR image of a single subject (see Fig. 2). Our interest focuses on the internal nuclei, which are segmented in the phantom. First, the atlas must be aligned to our set of images, which have been previously registered to the MNI atlas. Thus, we register the Zubal Phantom to the MNI template, again using the block-matching algorithm [37], to estimate an affine transformation. We perform a nearest-neighbor interpolation to preserve the segmentation labels. Fig. 2 shows the results of registering the Zubal Phantom on the MNI reference without disrupting the Zubal labels.

The Zubal Phantom does not include labels for the thalamic nuclei, such as the pulvinar. According to Talairach and Tournoux [45], the pulvinar represents the "large posterior portion of the thalamus," which is "limited by a conventional verticofrontal plane through the posterior commissure" (CP). This plane (VCP) goes through the ventricular margin of CP and is perpendicular on the CA–CP biocommissural line of Talairach. We draw VCP as described above and the result is shown in Fig. 5 left, where the pulvinar is marked in black. In Fig. 5, right, we represent in black what we call "anterior thalamus," an area in the anterior part of the thalamus (above the VCP plane), which is used to compute mean values of deep GM in a region with very low probability to show hyperintensities in CJD patients.

B. Detection of Internal Nuclei and Refined Segmentation

Once the Zubal Phantom is registered to the working framework, we can easily depict the brain structures that are of interest, namely the deep GM internal nuclei. Reports in literature [5], [15], [21], [51], [52] mention the importance of analysing MR intensities in the basal ganglia. Hence, we create a mask with the thalamus, putamen and head of the caudate—which will be referred to as internal nuclei for the rest of this paper—from the Zubal Phantom registered on MNI. We aim to use this mask for the segmentation of internal nuclei in patient images. Although the affine registration gives correct correspondences in a general brain registration framework, the anatomical variability between patients makes the

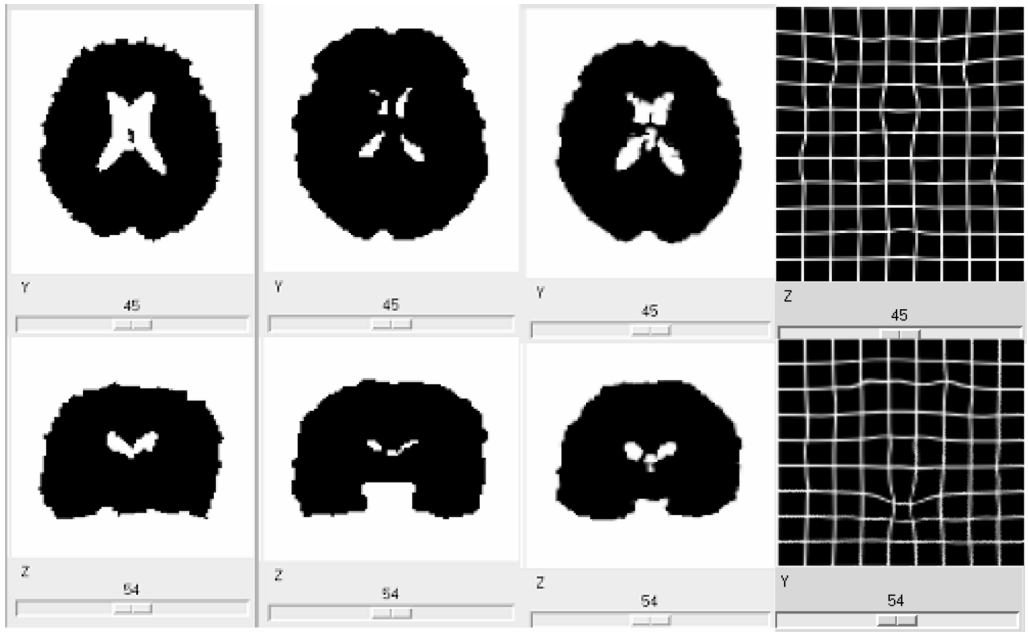

Fig. 6. Registration of the Zubal ventricle and cortex outer boundary on a patient with very large ventricles. This is the most difficult case encountered. Patient has brain atrophy and dilated ventricles, while the ventricles of the Zubal Phantom are small. From left to right: column 1, the ventricles and brain margin of the patient (ventricles segmented from T2 and cortex from T1); column 2, the ventricles and brain boundary of Zubal Phantom; column 3, the ventricles and cortex boundary of the Zubal Phantom registered to the patient; column 4, the deformation fields of the nonrigid registration.

correspondence between the Zubal internal nuclei mask and the corresponding internal nuclei in each patient erroneous. A refinement of the registration in the deep GM between the Zubal internal nuclei mask and the patient internal nuclei seems necessary.

The segmentation of internal nuclei in patient images is not an obvious task; nevertheless, there are other important anatomical landmarks in the brain that are easier to identify. We concentrate on the segmentation of ventricles and cortex external boundary. Ventricles will give a good approximation of the deformation field around the internal nuclei, whereas the cortex boundary will impose global spatial constraints and stabilize the deformation field inside the brain.

To obtain similar images of segmented brain margin and ventricles for each patient, we employ morphological opening [42], two erosions followed by two dilations, to extract the ventricles from T2 (with higher contrast between CSF and brain) and the cortex from T1 patient images. The cortex boundary could normally be extracted from either T1 or T2 sequence; we prefer to use the T1 sequence, since the T2 images we use lack some top and bottom slices. Although the ventricles are located in the middle of the brain and it is correct to extract them from T2 images, the cortex would be incomplete. In both cases, we used the original nonregistered images. The segmentation results are registered to the MNI by applying the transformations computed for the corresponding T1 and T2 images.

We are now in possession of two binary maps of ventricles and brain boundaries for each patient: one from the Zubal Phantom and the other from the patient. Nonrigid registration is used to align the two images, employing the iconic feature-based algorithm described in [7]. Fig. 6 shows typical registration results and the related three-dimensional deformation fields. The outer margin of the cortex ensures that the deformation fields are spatially sound and do not pull the internal nuclei over their location.

We apply the computed deformation fields to the mask of internal nuclei of the Zubal Phantom, deforming the mask according to the position and size of the ventricles in the patient image. The deformed mask is used to segment the internal nuclei on the patient image.

The nonrigid registration is done between the segmented binary masks of ventricles and cortex boundary; hence it should allow maximum deformation to find the best fit between the pair of ventricles and brains. The resulting transformation conveys the deformation that must be applied to the Zubal phantom (or its segmented internal nuclei), already registered to MNI, to fit any of the patients MRI modalities, given that they are also registered to MNI. Since we use only the shape of ventricles and cortex as registration constraints, the transformation will take into account neither pathology in the grey or white matter nor other differences between scans or brain anatomies.

Fig. 7 shows an example of internal nuclei registration and the segmentation results in a T1-weighted MR image of a patient. The segmentation of internal nuclei is important for discarding possible false positives (FPs) in the detection of hyperintensities. In Fig. 8 we show more details about the segmentation of internal nuclei by browsing through the MR slices (i.e., axial, coronal, and sagittal) of a patient.

C. Adaptive Thresholding

A foveal segmentation algorithm completes the detection of areas of CJD MR hypersignals in the brain. This method was previously applied with success to the early detection of microcalcifications in mammography [30], [31]. This is in essence an

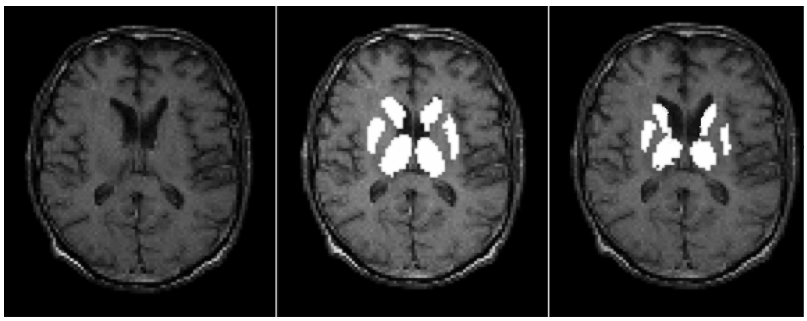

Fig. 7. Example of internal nuclei segmentation in a T1-weighted image of the patient with very low contrast. On the left, the T1 image of the patient. In the middle, the segmentation of internal nuclei according to the internal nuclei binary map before nonrigid deformation with the head of the caudate superposed on the ventricles. On the right, after nonrigid deformation, showing an accurate segmentation.

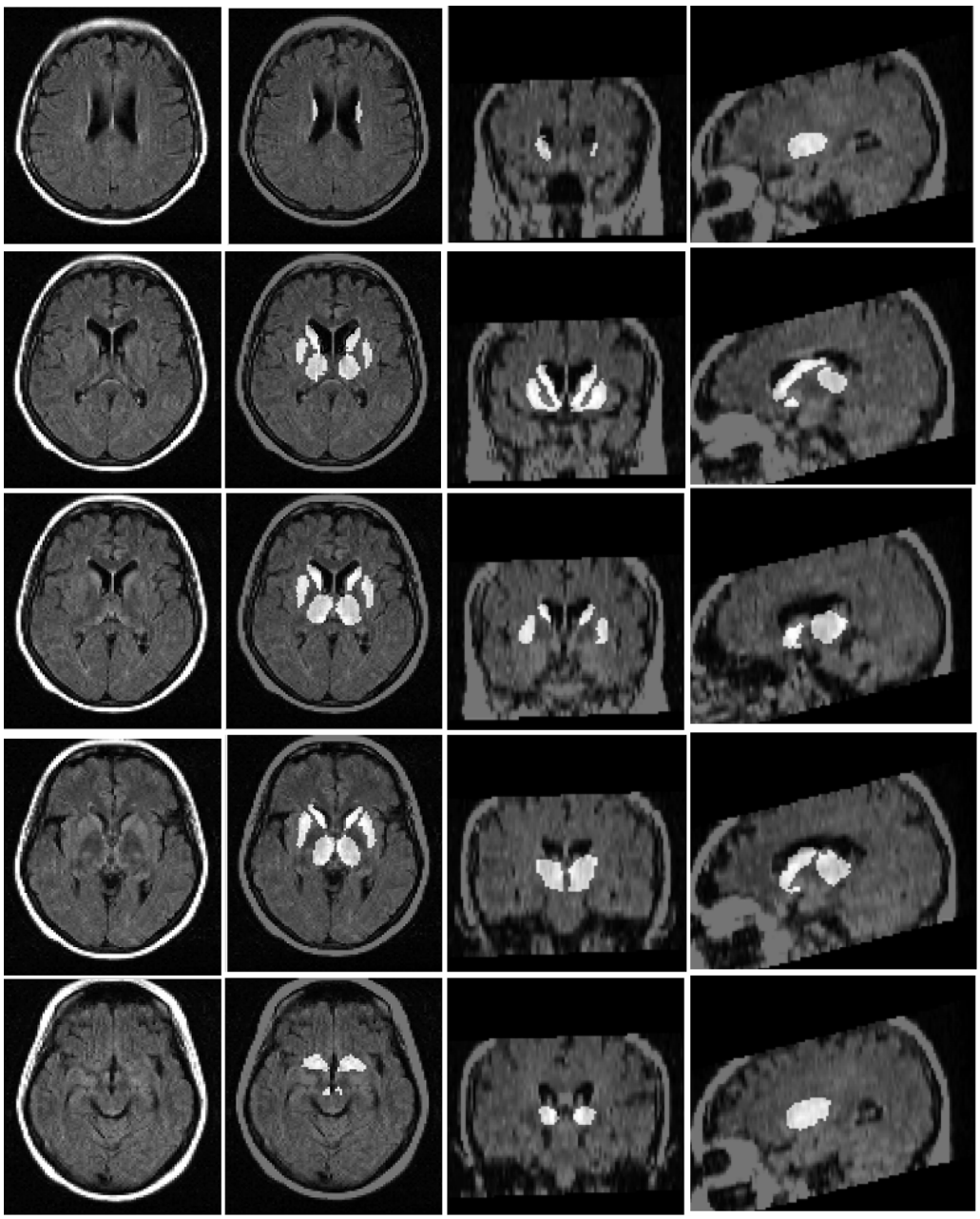

Fig. 8. Another example of internal nuclei segmentation in a T1-weighted image of the patient. In the far left column, we present the axial T1 slices of the patient. In the inner left column, the segmentation of internal nuclei in the corresponding axial slices. In the inner right column, the segmentation of internal nuclei in coronal MR slices; while in the far right column, the segmentation results in sagittal MR slices.

algorithm of adaptive thresholding, which uses a mathematical model of human vision. Its motivation comes from the better sensitivity and specificity that the human eye has over classical algorithms in detecting and characterizing image features.

We compute a set of mean values using masks for the object area (O), its neighborhood (N: the local area around the object), and background (B: the rest of the brain), as in (3), where π represents the number of voxels in the area. μ_A, the adapted mean, is calculated as in (3), where w is a suitable weight between 0 and 1 affecting the amount of background implied in the computation of contrast. The perceivable contrast C is calculated according to (4)

$$\begin{aligned}\mu_o &= \frac{1}{\pi_o}\sum_{i\in\delta_o} I_i \\ \mu_N &= \frac{1}{\pi_N}\sum_{i\in\delta_N\setminus\delta_o} I_i \\ \mu_B &= \frac{1}{\pi_B}\sum_{i\in\delta_B} I_i \\ \mu_A &= w\mu_N + (1-w)\mu_B \qquad (3)\end{aligned}$$

$$C = \begin{cases} \frac{\mu_o-\mu_N}{\mu_N}, & \text{if } \mu_o > \mu_N \\ 0, & \text{otherwise} \end{cases} \qquad (4)$$

$$C_{\min} = \frac{c_{\mathrm{mpc}}}{\mu_N}\left(b + \sqrt{\frac{\mu_N^2}{\mu_A}}\right)^2. \qquad (5)$$

We then compute the adaptive threshold $C_{\min}$ shown in (5), where c_{mpc} is the minimal perceivable contrast by maximum illuminance. b is a constant regulating the normalized amount of light that discriminates an object from the background. We used the value $b = 0.808$ proposed in [34]. Using $C_{\min}$, the contrast is adapted locally, not only globally, in a manner similar to that of HVS. Areas in the brain image having $C > C_{\min}$ are marked as hyperintensities.

As argued in [31], the minimal perceivable contrast must be computed as a function of the image gradient in order to accommodate all possible variations of contrast. In MR images of the brain, the intensity values of GM, WM, and CSF can be regularised by intensity normalization. Therefore, hyperintensities can be regarded as an exception to the normal intensity distribution; in this particular case (after image normalization), a constant c_{mpc} over the whole database gives good segmentation results. Depending on image quality and movement artefacts, there will still exist some contrast variability especially between GM and WM and from one image to another. Using an adaptive contrast measure both locally and globally, through the HVS foveal segmentation, our algorithm is less sensitive to such artefacts and image quality.

D. Intensity Quantitative Analysis

With the tools developed in this study, we can perform what seems to be the first computer-aided quantitative analysis between intensities in caudate nuclei or putamen, on one hand, and thalami (pulvinar nuclei and anterior thalami), on the other hand, for CJD patients. We will refer to it as intensity quantification study (IQS).

We use the segmented putamen, caudate nuclei, pulvinar, and anterior thalami on the patient images to compute the mean MR intensities in nuclei, as observed in FLAIR images. We calculate the absolute values of the subtraction between the mean intensities in either putamen or caudate nuclei and the mean intensity in pulvinar and compare them with the maximum over all controls. We calculate the absolute values Δ_1 and Δ_2 as in (6) to represent the mean intensity differences for each patient and control, where $\overline{\mathrm{Pul}}$, $\overline{\mathrm{Put}}$, $\overline{\mathrm{CN}}$, and $\overline{\mathrm{AT}}$ represent the mean intensities respectively in the pulvinar, putamen, caudate nuclei, and "anterior thalamus." M represents the maximum value of all Δ_1 and Δ_2 over all controls. Δ_1 and Δ_2 express quantitatively the clinical observations regarding MR intensity differences in CJD patients

$$\begin{aligned}\Delta_1 &= |\overline{\mathrm{Put}} - \overline{\mathrm{Pul}}| \\ \Delta_2 &= |\overline{\mathrm{CN}} - \overline{\mathrm{Pul}}| \\ M &= \max_{\mathrm{controls}}(\Delta_1, \Delta_2). \qquad (6)\end{aligned}$$

We define a first CJD prompting ratio CP for the separation of CJD patients from healthy cases as in (7). CP reflects the value in each control that is closer to the patient data and therefore less discriminating, while in patients it highlights the most suspicious grey nuclei (as not all nuclei are affected in a patient and different types of CJD affect different nuclei more strongly). CP is expected to differentiate between CJD patients and controls, based on the clinical observations that found abnormal MR intensities in at least one of the pulvinar, putamen, and caudate nuclei

$$\mathrm{CP} = \max_{\mathrm{case}}(\overline{\mathrm{Pul}}/\overline{\mathrm{AT}}, \overline{\mathrm{Put}}/\overline{\mathrm{AT}}, \overline{\mathrm{CN}}/\overline{\mathrm{AT}}) \qquad (7)$$

$$\mathrm{CC} = \overline{\mathrm{HCN}}/\overline{\mathrm{HPul}}. \qquad (8)$$

We further define a first CJD characterisation ratio CC, as in (8), where $\overline{\mathrm{HPul}}$ and $\overline{\mathrm{HCN}}$ represent the mean hyperintense (abnormal) values (lesion specific) in the pulvinar and caudate nuclei. Using the conclusion of clinical studies, we aim to use CC to differentiate between sCJD and vCJD, based on the lesions topographical distribution.

IV. Results

A. Data

The data collected for the GIS-Prions Project were acquired in two major neuroradiological centers of France: the Pitié-Salpêtrière Hospital in Paris and the Timone Hospital in Marseille. The database contains MR sets for a total of 25 subjects: 10 sCJD cases (five definite and five probable cases); five vCJD cases (two definite and three probable cases with detection of PrPres in tonsil biopsy); and 10 healthy controls, which are used for the validation of the algorithm. The ages of sCJD patients vary between 55 and 79 years with an average of 64 years, while the vCJD vary between 18 and 52 years with an average age of 36 years. The average age of all patients is 54 years. The ages of controls vary between 31 and 68 with an average age of 50 years. There may be effects of aging, but they are not fully understood. There is *a priori* no reason to

TABLE I
MEAN VALUES OF INTENSITY, STANDARD DEVIATION, Δ_1 AND Δ_2 IN PULVINAR, PUTAMEN, CAUDATE NUCLEI AND "ANTERIOR THALAMI" FOR THE PATIENT DATA. WE PRESENT RESULTS ON IMAGES BEFORE INTENSITY NORMALIZATION IN ORDER TO PRESERVE THE ORIGINAL INTENSITY VALUES; THEREFORE WE SEPARATE THE PARIS AND MARSEILLE DATABASES. ALL THE SCJD DATA ("S") SHOW HIGHER INTENSITIES IN THE CAUDATE AND SOMETIMES PUTAMEN (USUALLY BOTH), WHICH VERIFIES REPORTS IN THE LITERATURE. VCJD CASES ("V") SHOW HIGHER INTENSITIES IN THE PULVINAR TOO. NO ABNORMAL INTENSITIES ARE SIGNALLED IN THE INTERNAL NUCLEI OF CONTROLS ("C"). WE PRESENT THE RESULTS GROUPED BY THE TYPE OF DISEASE (SCJD AND VCJD), WHERE "PARIS-CJD" ACCUMULATES ALL THE PARIS CJD PATIENTS

CJD Type	PULVINAR		PUTAMEN			CAUDATE			ANTERIOR THALAMUS	
	Original FLAIR									
	Mean	STD	Mean	STD	Δ_1	Mean	STD	Δ_2	Mean	STD
Paris – s	125.53	18.40	138.26	26.65	12.71	144.18	40.51	18.66	111.03	21.33
Paris – v	147.74	27.90	144.10	18.73	15.96	147.00	31.60	12.40	125.84	22.26
Paris –CJD	135.62	22.71	140.91	23.05	14.18	145.46	36.46	15.81	117.76	21.75
Paris – c	112.40	11.78	107.84	11.912	4.72	114.24	21.22	3.08	106.16	12.40
Marseille – s	364.95	48.97	399.27	55.35	34.3	437.87	88.65	72.90	323.65	79.80
Marseille – c	374.42	46.59	364.21	39.39	10.21	388.15	63.02	13.74	342.09	57.27

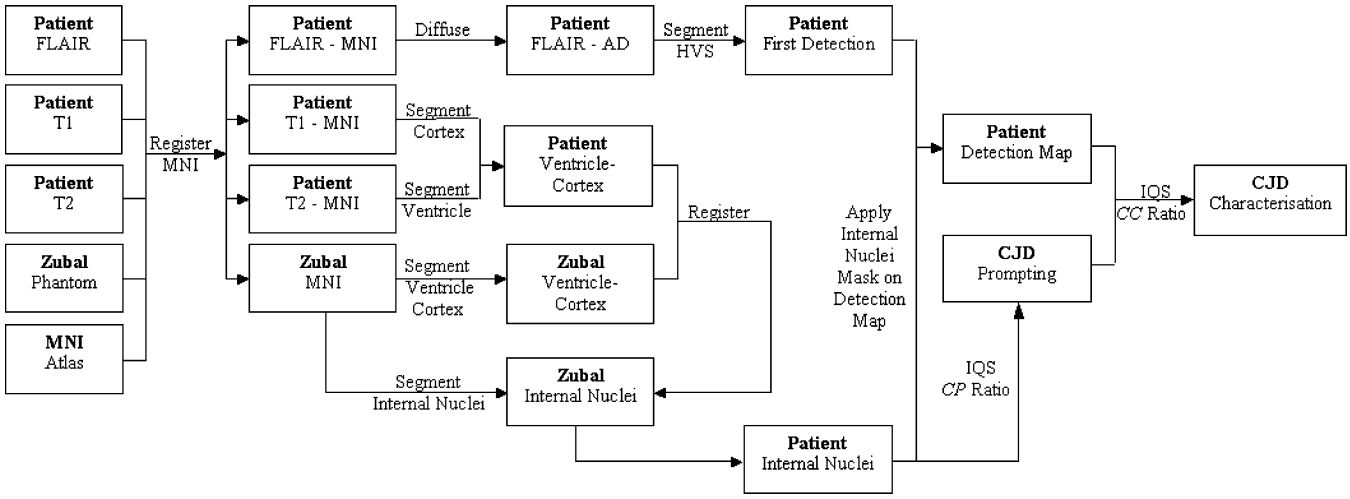

Fig. 9. Flowchart of the algorithm proposed for the detection and quantification of CJD-related abnormal hyperintensities in multisequence MRI of the brain.

find hyperintensities in FLAIR on different sites as a correlate of age.

The images collected at the Pitié-Salpêtrière Hospital in Paris were acquired using a 1.5 T GE Signa scanner. We use T1-weighted (TE = 20, TR = 500), T2-weighted (TE = 92, TR = 3000), and FLAIR-T2 (TE = 148.5, TR = 10002, TI = 2200) MR images. The CJD data collected at the Timone Hospital in Marseille were acquired using a 1.5-T Siemens Magnetom Vision scanner. We use T1-weighted (TE = 15, TR = 644), T2-weighted (TE = 22, TR = 4000), and FLAIR-T2 (TE = 110, TR = 8000, TI = 2200) MR images. First, we present results of hyperintensity detection. Subsequently, we show the results of the intensity quantification study (IQS).

B. Segmentation Results

In this part of the section, we show examples of detection of abnormal hyperintensities in FLAIR MR images of CJD patients. The MR scanners used in the two neuroradiological centers are from different manufacturers and the acquisition protocols differ slightly; our aim is to address all data in a common normalized framework. Although the raw intensity values in the two subdatabases are different (see Table I), through intensity normalization and the use of normalized ratios we can treat all data together in a nonparametrical framework for both hypersignal segmentation and intensity quantification. For each patient, we have a T1-weighted, a T2-weighted, and a T2-FLAIR sequence. In the examples shown below, we used all three MR imaging sequences for the registration of images and segmentation of hyperintensities. A review of the different stages of our segmentation algorithm is shown in Fig. 9.

For the validation of the segmentation of internal nuclei, an expert neuroradiologist manually segmented the head of the caudate, putamen and thalamus into seven MR FLAIR volumes (slice by slice). The sample database contained healthy individuals and CJD patients from both Paris and Marseille centers. The results were compared with those obtained by our

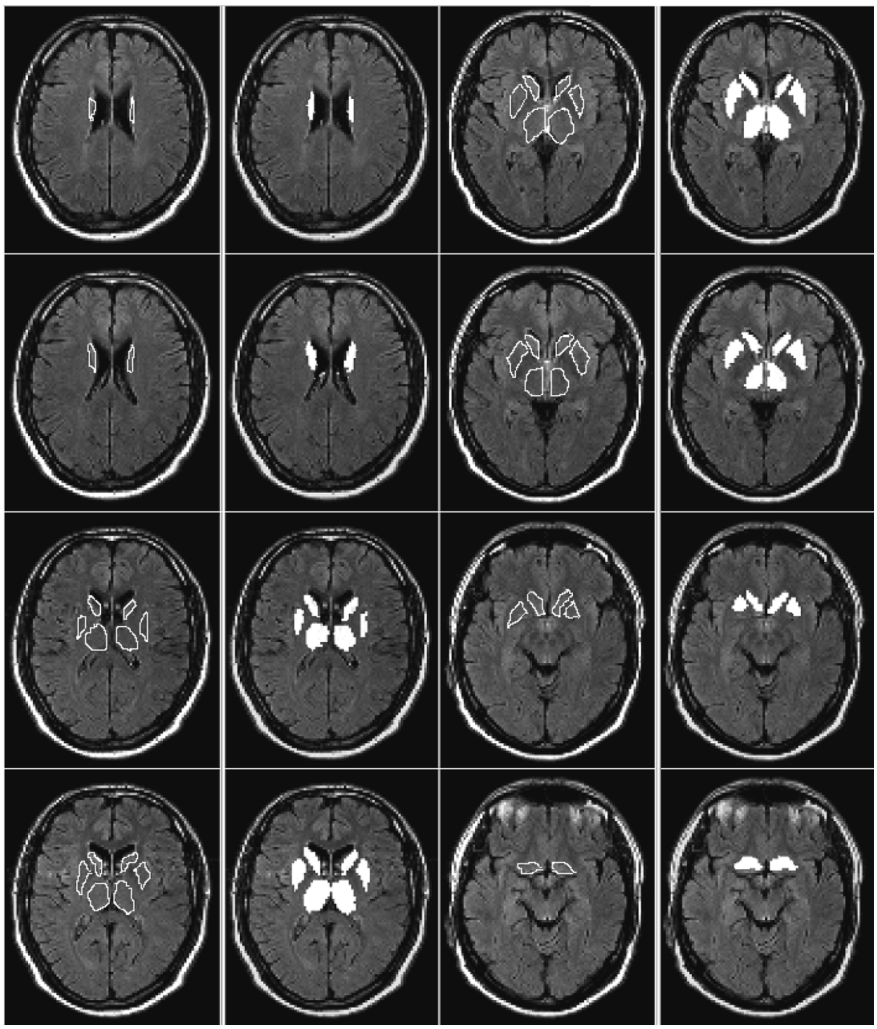

Fig. 10. Example of manual versus automatic segmentation of internal nuclei in a normal FLAIR image. In the left hand columns, the manual segmentation of the head of caudate, putamen, and thalamus done by an expert neuroradiologist. In the right hand columns, the automatic segmentation of internal nuclei done by our method.

automatic method to segment internal nuclei. The automatic segmentation is accurate and has excellent specificity. All the automatically segmented volumes are within the real internal nuclei. Conversely, the automatic segmentation underestimates slightly the size of certain internal nuclei: 2/7 of the posterior putamen and 3/7 of the posterior thalamus. The head of the caudate is correctly estimated in all cases. Fig. 10 shows some comparative results between the manually and automatically segmented nuclei.

The segmentation is done on the whole brain image, as the foveal thresholding is better adapted at the global level when applied to the whole brain, while the local adaptability is not altered. Using the mask of internal nuclei, we focused on the basal ganglia and did not take into account signal abnormalities in other brain regions, such as WM high signals that are known to correlate with age and vascular risk factors. Fig. 11 shows detection results on two patients with postmortem neuropathologically confirmed sCJD. The main radiological characteristic of the ten sCJD patients is the presence of higher intensities in the caudate nuclei and putamen. This is not always the case of thalami, where if there are hyperintensities they are lower than in putamen or caudate nuclei. Our algorithm detects abnormal hyperintensities in all 10 sCJD cases. Note the asymmetry of high signals in the first case in Fig. 11.

The detection of hyperintensities in vCJD cases is further shown in Fig. 12. Strong thalamic abnormal intensity distributions are present in all cases. The most affected thalamic nucleus is the pulvinar and we note that hyperintensities do not spread all over the thalamus and are localised in the posterior and dorsomedial thalamic areas, which gives the "hockey-stick" appearance of the hypersignals, as in Fig. 12. Our algorithm detected abnormal hyperintensities in all five vCJD cases. None of the internal nuclei are generally affected entirely (usually only parts of them show abnormal hyperintensities), therefore, the need to concentrate on the hyperintense areas, rather than the entire nucleus.

When applying our algorithm on the 10 healthy controls, no hyperintensities are detected in nine of these images. A motion artefact leads to a FP in one control image, which lies within the left thalamus, but outside the pulvinar area.

The detection of abnormal intensities in basal ganglia is consistent over both databases from Paris and Marseille, although the acquisition protocols vary, as well as the MR scanners used

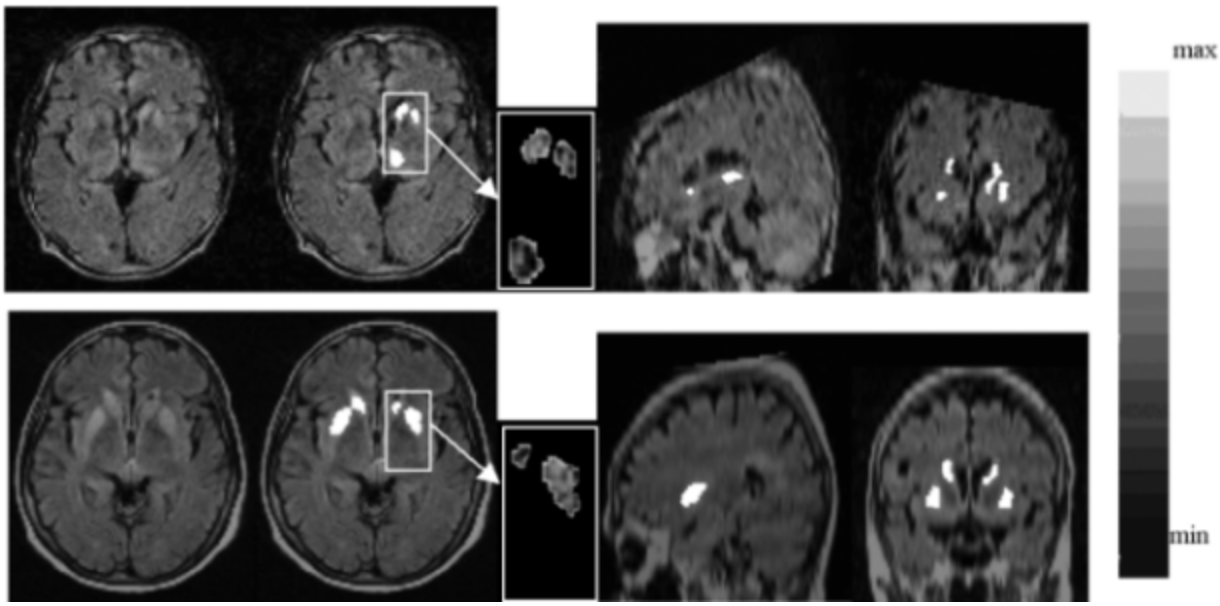

Fig. 11. Results on patient data—sCJD cases. Both sets of images reported above (one row per case) originate from patients with definite sCJD. On the left, we present a cross section of the FLAIR MR data with abnormal hyperintensities in the internal nuclei. Next to it we have the CJD detection map with corresponding intensities, as seen in the attached colourmap. Further to the right, we present a sagittal cross section and a coronal cross section with their detection maps. Top row case originates from the Paris database. Bottom row case is from the Marseille database.

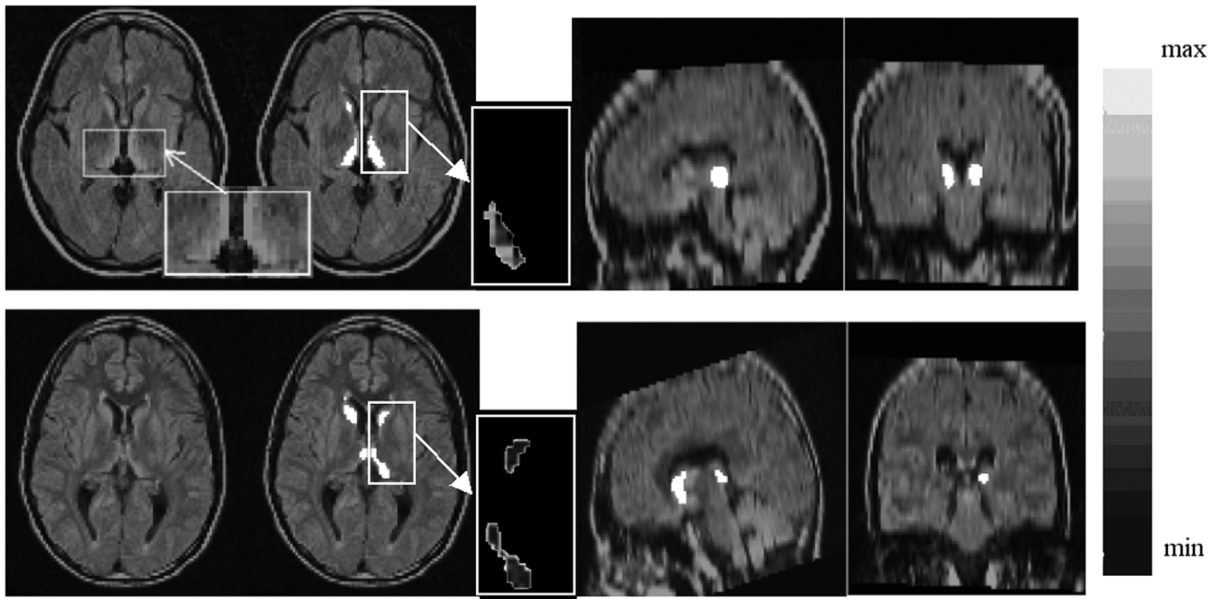

Fig. 12. Results on patient data—vCJD cases. Both sets of images reported above (each case is reported on a separate row) originate from patients with definite vCJD. On the left, we present a cross section of the FLAIR MR data with abnormal hyperintensities in the internal nuclei. Next to it, we have the CJD detection map with corresponding intensities, as seen in the attached colormap (note the high intensities present in the thalamic area). Further to the right, we present a sagittal cross section and a coronal crosssection with their detection maps. On the top row case on the left, we show a magnified image of the "hockey stick" shaped thalamic hyperintensities characteristic to vCJD. Both cases originate from the Paris database.

to obtain the data. Through spatial registration and intensity normalization, our algorithm is not sensitive to original imaging conditions and offers good results over all data.

C. IQS Results

For the IQS, we prefer using FLAIR images before intensity normalization for the most accurate estimation of mean values in the segmented internal nuclei. In fact, normalization was required to make the segmentation of hyperintensities nonparametric, but it is not required for IQS, since it is based on ratios that implicitly normalize the data. This naturally leads to different intensity values for the Paris and Marseille databases, which were acquired with different MR scanners and protocols. We present in Table I, along the mean intensities and standard deviations grouped by type of disease (or control) and type of nucleus, the values of Δ_1 and Δ_2 [from (6)]. The values of M are 9.48 for the Paris data and 25.63 for the Marseille data.

As expected, there is no significant difference between mean intensities in putamen or caudate nuclei versus pulvinar for our control data. We performed a nonparametric two-sample

TABLE II

NORMALIZED MEASURE TO DIFFERENTIATE CJD PATIENTS FROM CONTROLS. FOR EACH CJD PATIENT AND CONTROL IN THE DATABASE, WE DIVIDE THE MEAN COMPUTED INTENSITY VALUES IN THE PULVINAR, PUTAMEN AND CAUDATE NUCLEUS BY THE MEAN INTENSITY VALUE IN THE "ANTERIOR THALAMUS." FOR CONTROLS ("C"), THE COMPUTED NUMBER MUST BE CLOSER TO THE IDEAL VALUE OF 1, WHICH WOULD REFLECT NO VARIATION IN INTENSITY OVER THE DEEP GREY NUCLEI. TABLE SHOWS IN BOLD THE VALUES THAT ARE HIGHER THAN THE LARGEST NUMBER OVER ALL NUCLEI AND OVER ALL CONTROLS. ALL 10 SCJD ("S") PATIENTS SHOW HIGH RATIOS RELATED TO THE CAUDATE NUCLEUS AND 8/10 RELATED TO THE PUTAMEN, WHICH SEPARATE THEM FROM CONTROLS

CJD Type	Pulvinar/ Anterior Thalamus	Putamen/ Anterior Thalamus	Caudate/ Anterior Thalamus	CJD Type	Pulvinar/ Anterior Thalamus	Putamen/ Anterior Thalamus	Caudate/ Anterior Thalamus
PS001 – s	1.0832	**1.3001**	**1.2927**	**PS018 - v**	**1.2325**	**1.1713**	**1.2239**
PS005 – s	1.1223	**1.1852**	**1.2159**	**PS019 – v**	**1.1634**	1.0496	1.0712
PS006 – s	1.0653	1.0892	**1.1616**	**TP001 – c**	1.0830	1.0033	1.0732
PS008 – s	1.1058	**1.2375**	**1.2550**	**TP002 – c**	0.9713	0.9741	0.9981
PS009 – s	**1.2387**	**1.4322**	**1.4683**	**TP003 – c**	1.0759	1.0327	1.0643
PS013 – s	1.1516	**1.2248**	**1.3733**	**TP004 – c**	1.0894	1.0009	1.0785
MT001 – s	1.1525	**1.3133**	**1.3151**	**TP005 – c**	1.0757	1.0585	1.1547
MT008 – s	**1.1994**	**1.4000**	**1.3938**	**TM001 – c**	1.1270	1.0937	1.1427
MT009 – s	1.1271	**1.1770**	**1.2485**	**TM002 – c**	1.0528	1.0525	1.0823
MT012 – s	1.0442	1.0660	**1.1666**	**TM003 – c**	1.1173	1.0440	1.0927
PS015 – v	**1.1711**	0.9740	1.0232	**TM004 – c**	1.0873	1.0730	1.1317
PS016 – v	**1.1989**	**1.3082**	**1.2763**	**TM005 – c**	1.0894	1.0617	1.1363
PS017 - v	1.1105	**1.2369**	**1.2563**				

Kolmogorov–Smirnov (KS) test [1] under the null hypothesis that the distribution of caudate, and respectively putamen, intensities is similar to that of pulvinar. The hypothesis is accepted for the Paris control at a significance value of 0.99 for caudate, respectively, 0.69 for putamen. For the Marseille control data, the significance value is of 0.53 for caudate, respectively, 0.42 for putamen.

The results in Table I are consistent over the sCJD patients and conform to the clinical observations. All sCJD cases have a clear higher signal in the caudate (in 10/10 cases), while the putamen in 6/10 cases. vCJD data present very high intensities in the pulvinar, although hypersignals may be present in the putamen and caudate nuclei too. At this stage, we used mean values over the entire nucleus, while hyperintensities are not homogeneous and usually present only in parts of the affected nucleus. Hence, a study of hyperintensities, rather than mean nucleus intensities seems appropriate, as shown later in the paper. We note that all CJD cases have higher Δ_1 and Δ_2 values than controls (see M).

1) CJD Prompting: Intensity values in Table I are different for the Paris and Marseille data, due to the different scanners and protocols used in the neuroradiological centers where our data were acquired. In Table II, we introduce a normalized measure for our database. We divide the mean intensity values in the pulvinar, putamen, and caudate nuclei over the mean values in the "anterior thalami" of each patient and control. We highlight in bold characters the values in patient data that are greater than the highest value of all ratios over the control data (which is 1.155). All patient data provide at least one suspicious value (in bold) higher than 1.155. By choosing the largest value over the ratios of controls as threshold, we prohibit the occurrence of FP in separating patients from controls, but do not exclude the prompting of false negatives (FN).

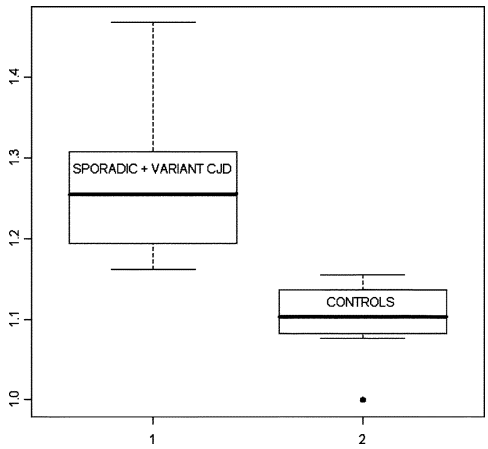

Fig. 13. Box plot of the two groups: 1) CJD patients (on the left), including the sCJD and vCJD cases; 2) controls (on the right). Vertical axis shows the CP ratio. Group medians are shown as central bold lines and the outlier as filled circle. Although the maximum value in the control group and the minimum value in the patient group are very close, the two groups have very distinctive distributions.

All 10 sCJD cases show high values in the caudate ratio, as well as 8/10 in the putamen ratio. Four out of five vCJD cases present high values in the pulvinar ratio, while 3/5 in the putamen and caudate nuclei, when mean intensities (not hyperintensities) over the entire nucleus are computed.

We box plot the value of CP into two groups: 1) CJD cases (sporadic and variant together) and 2) controls, as shown in Fig. 13. For each group of data (CJD patients or controls), the plot shows the group median value (the bold central line), the

TABLE III
NORMALIZED MEASURE TO DIFFERENTIATE sCJD CASES FROM vCJD. THE TABLE SHOWS IN BOLD THE CC VALUES THAT ARE GREATER THAN ONE, WHICH IS THE CASE OF ALL 10 sCJD PATIENTS. IN ITALIC WE PRESENT THE CC VALUES SMALLER THAN 1, WHICH IS TRUE FOR ALL vCJD CASES. WHEN THERE ARE NO HYPERINTENSITIES DETECTED, WE MARKED "NO PULVINAR" OR "NO PUTAMEN," ACCORDING TO THE UNAFFECTED NUCLEUS.

CJD Type	HPutamen/ HPulvinar	HCaudate/ HPulvinar	CJD Type	HPutamen/ HPulvinar	HCaudate/ HPulvinar
PS001 – s	**1.2310**	**1.2440**	**MT009 – s**	**1.0971**	**1.0983**
PS005 – s	**No pulvinar**	**No pulvinar**	**MT012 – s**	**1.0918**	**1.1015**
PS006 – s	**1.0609**	**1.0845**	**PS015 - v**	No putamen	*0.9506*
PS008 – s	**1.2301**	**1.1981**	**PS016 - v**	*0.9833*	*0.9990*
PS009 – s	**1.1448**	**1.2610**	**PS017 - v**	*0.9762*	*0.9915*
PS013 – s	**1.1168**	**1.2772**	**PS018 - v**	*0.9753*	*0.9952*
MT001 – s	**1.1661**	**1.1721**	**PS019 – v**	*0.9292*	*0.9028*
MT008 – s	**1.0816**	**1.1927**			

minimum and maximum values (at the end of the dotted lines), the upper quartile (the median of the upper half of data), and lower quartile (the median of the lower half of data), which enclose the box around the median, and the outliers (in circles). Performing a Welch two sample t-test [8] between the two groups we get a value of $p = 5.7 * 10^{-6}$, which gives an excellent separation between patients and controls. The ratio mean values are 1.266 for CJD patients and 1.101 for controls. There is one outlier (shown as a circle in Fig. 13), corresponding to one control (TP002), which presents extreme values. The CP ratio achieves simultaneously zero FP and zero FN in prompting CJD.

Given the small number of cases, and that the CP values are ratio values, we performed a nonparametric two-sample KS goodness-of-fit hypothesis test [1] on the CP ratios, under the null hypothesis that the distribution of CJD patients is the same as that of normals. The hypothesis was rejected with an asymptotic p-value of $2.3 * 10^{-6}$. With 15 patients and 10 normals $((15 * 10)/(15 + 10) = 6 > 4)$ the p-value is of sufficient accuracy.

In this experiment, simple discrimination was successful, as there was no overlap between the CP distributions of patient and control data. In more complex cases, in which such an overlap may occur and the relative risk associated with FP and FN increase, we would need to resort to discriminant analysis techniques [16].

2) CJD Characterisation: We showed how CJD patients could be separated from controls using mean intensity values from pulvinar, putamen and caudate nuclei and their relation with the mean intensity within the "anterior thalamus". Not all the addressed internal nuclei show hyperintensities for all patients (as seen in Fig. 11 and Fig. 12), as the pulvinar or the putamen may not always present abnormal distributions; the caudate appears to be the only nucleus constantly affected. Furthermore, only parts of a nucleus may show hyperintensities and, therefore, the mean value computed over the entire nucleus does not always reflect the degree of abnormality in the respective nucleus. It is important to compute mean intensities over the entire nucleus (i.e., pulvinar, putamen, or caudate) to be able to distinguish patients from controls (who have no hyperintensities in the deep grey nuclei). But nucleus mean intensities are insufficient to characterise the CJD type.

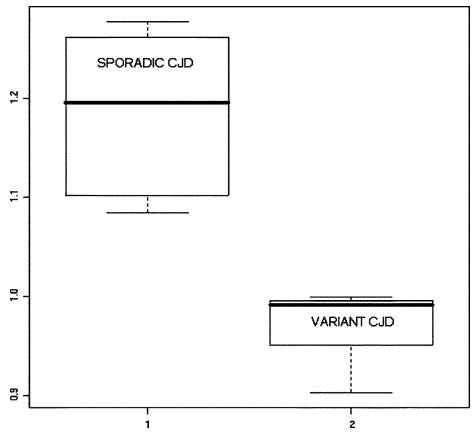

Fig. 14. Box plot of the two groups: 1) sCJD patients (on the left); 2) vCJD cases (on the right). Vertical axis shows the results of the CC ratio, as in Table III. Group medians are shown with a bold central line; there are no outliers. Plot shows very distinctive distributions for the two groups.

The ground truth states that sCJD and vCJD patients have different lesion topographies, with higher abnormal MR intensities (thus, hyperintensities) in the pulvinar in vCJD cases [36], [51]. Hence, we highlight the relation between pulvinar and caudate MR hyperintensities to differentiate sCJD from vCJD. The abnormal intensities we will refer to are the hyperintensities found by our detection algorithm based on a HVS model (cf. Section III-C).

We employ masks as shown in Figs. 11 and 12 and compute mean intensity values only over the hyperintense areas. This allows us to study the relation between the abnormal intensities detected in the caudate nuclei of patients (which are relevant in each patient, as seen in Table II) and their pulvinar (as the pulvinar is the nucleus that can discriminate sCJD cases from vCJD).

We present the ratios between hyperintensities in caudate/putamen and pulvinar in Table III. When there is no hypersignal in the nucleus, this is marked as "no pulvinar" or "no putamen," whether the nucleus is the pulvinar or the putamen. In bold numbers, we present values greater than 1, while numbers lower than 1 are shown in italic. All 10 sCJD cases are shown in bold values, while all five vCJD cases are presented in italic.

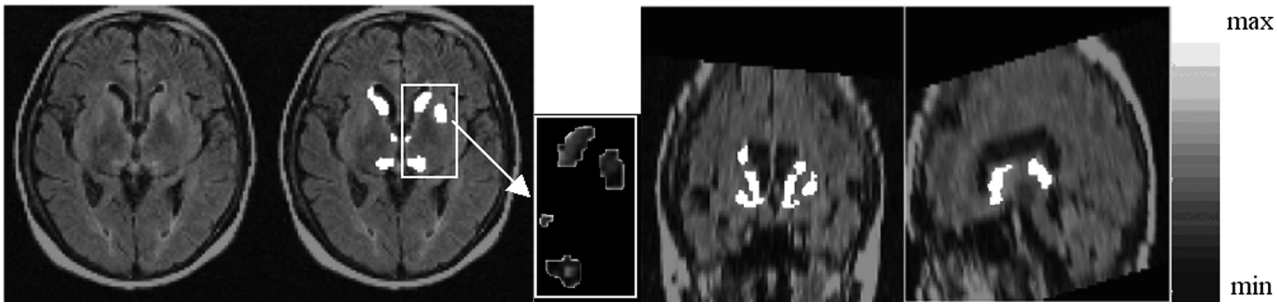

Fig. 15. Hyperintensity detection results on a case where the characterisation of the type of CJD by clinical visual interpretation of MR intensities was difficult. After the detection of hyperintensities and quantification of intensities, our algorithm classifies the case correctly as vCJD, as certified by biopsy.

Table III demonstrates the utility of IQS to separate the two subgroups of CJD patients: sCJD and vCJD. Furthermore, these results prove in a quantitative form that vCJD patients present higher abnormal intensities in the pulvinar than putamen or caudate nuclei, whereas sCJD patients show stronger hyperintensities in the caudate nuclei or putamen than pulvinar.

The box plot of the two patient subgroups is presented in Fig. 14. When no pulvinar hyperintensity was detected (see PS005), we input instead the maximum value over the other sCJD cases, namely 1.277. This conservative choice minimizes the ratios and avoids division by zero in cases when $\overline{\mathrm{HPul}}$ is null. The two distributions are clearly different, as shown by the result of the Welch two sample t-test with a p value of $5.8 * 10^{-6}$. The ratio mean values of the two classes are 1.190 for the sCJD and 0.967 for the vCJD.

We further performed a nonparametric two-sample KS test on the CC values, under the null hypothesis that the distribution of sCJD patients is the same as that of vCJD patients. The hypothesis was rejected with an asymptotic p-value of $6.3 * 10^{-4}$. Given the small database, with 10 sCJD patients and five vCJD cases $((10 * 5)/(10 + 5) = 3.33 < 4)$, the p-value is of relative accuracy.

The example shown in Fig. 15 refers to a case in which the characterisation of CJD type by visual inspection in the clinical environment was difficult, as sCJD can mimic vCJD [20]. The FLAIR MR image of this patient shows high abnormal intensities in the pulvinar, putamen and head of the caudate. After intensity quantification, the CC ratio is smaller than one, which indicates a vCJD case. The subsequent biopsy confirmed the result.

IQS first separates the CJD patients from healthy controls using the defined CP ratio. Once the CJD cases isolated, we use the CC ratio to discriminate vCJD from sCJD cases. Thus, IQS allows the unambiguous differentiation of three distinctive classes: healthy controls, sCJD patients, and vCJD patients.

We collected two series of results: one from the foveal segmentation of hyperintensities in the basal ganglia (HVS), and a second from the intensity quantification study (IQS) of intensity differences between putamen/caudate/pulvinar nuclei versus "anterior thalamus." Thus, our database comprises 15 patients consisting of 10 sCJD cases, five vCJD cases, and 10 controls. All patient MRI sets show hyperintensities in the zone of interest. With a combination of HVS and IQS, we are able to prompt 15/15 prion disease cases with simultaneously no FP and no FN. We detected all cases of hyperintensities in the basal ganglia employing the foveal segmentation of signal deviations.

V. Discussion

The results presented in Tables I–III represent a first attempt for automatic quantitative numerical analysis of MR intensities of pulvinar versus putamen and caudate nuclei in FLAIR-T2 images of CJD patients. They accurately quantify the clinical remarks related to the possible classification of different types of human spongiform encephalopathies.

The main contribution of this paper is the automation of the differential diagnosis and, in some cases, an improvement of the diagnosis itself. The original steps of our algorithm include the atlas-based segmentation of internal nuclei using anatomical landmarks, namely the ventricles and cortex boundary, aimed at segmenting brain images with very low contrast between white and grey matters and identifying specific anatomical segments of the brain in patient images. We also present an example of adaptive thresholding based on HVS, used for the first time in MR image analysis, the major advantage of which is its adaptability both locally and globally to varying contrasts in images. Our method further combines image normalization (spatial and intensity-based) with adaptive thresholding (foveal algorithm) and the definition of intensity-based ratios into a new tool toward the diagnosis of multiple forms of CJD by brain MRI.

We define two new MRI-based ratios to prompt and differentiate CJD forms. All patients show abnormal intensities in the deep grey nuclei, which are correctly detected by our algorithm. All 10 sCJD patients have higher mean intensities in the caudate nuclei and generally putamen. vCJD cases show higher hyperintensities in the pulvinar than in the other deep grey nuclei, which distinguishes from the sCJD cases. Sporadic cases may also show evidence of pulvinar hyperintensities and they can mimic variant cases [20], but these abnormal intensities are lower in magnitude when referred to the caudate and putamen intensities. All our experimental results are in complete accordance with the neurological findings in clinical practice and with the brain lesions profile described in each form of the disease. We did not detect any hyperintensities in the basal ganglia of controls (except for a movement artefact in the thalamus of one control found outside the pulvinar area), nor did we find significant differences between the mean intensities in their three deep grey nuclei of interest (pulvinar, caudate nucleus, and putamen).

In order to decrease the number of FP prompted by our segmentation algorithm, we refined the registration of the segmented data (the Zubal Phantom) on the patient specific data. To highlight the utility of using masks of the cortex outer boundary beside those of ventricles (see Section III-B), we also tested the use of masks of only ventricles (therefore, without regularising the deformation within the brain) with a clear advantage for using the brain boundary as an anatomical constraint. The results are again superior when noise is removed preserving edges. Due to space constraints and the consistency in the level of description of all the techniques involved, we do not report in this paper the details of these tests.

We investigated the response of well-known algorithms, such as VBM [1], [25] and EMS [47], to detect CJD-related abnormalities in brain MRI. Good contrast between brain structures is essential in statistically based methods. Hence, the performance of EMS and VBM on CJD patient data, which have important artefacts and no contrast between GM and WM, is inconsistent and irrelevant for clinical applications. Registration errors also influence the quality of statistical results, as comparisons between equivalent areas in normals versus patients or between different groups of patients are very sensitive to the correct delineation of the regions of interest. Please note that we employed the basic VBM version provided by SPM [2], using a mask of segmented GM to search lesions in GM only. Other options for VBM are available and might give better results, but this was not pursued in this paper. The effect of partial volume effects (PVE) [19] will also be investigated for removal of FP, along with the improved segmentation of ventricles by phase congruency (PC) [29].

The detection of deep grey nuclei hyperintensities confirms the previous visually based clinical observations according to which the FLAIR/T2 MR images of sCJD patients show hypersignals in the caudate nuclei. Quantifying the intensities in thalami, caudate nuclei, and putamen, we show that there are always higher mean intensities in the caudate nuclei (10/10) and sometimes putamen (6/10) than the pulvinar of sCJD patients. The caudate nucleus is also of high intensity in the vCJD cases. This conclusion highlights the caudate nuclei as an area of interest for the diagnosis of CJD, in complete agreement with the neuropathological findings.

The algorithm allows the study of asymmetries in CJD MR hypersignals, which has been long questioned by neuropathologists. Using basal ganglia masks, we also note that hypersignals are not homogeneous over the nuclei.

With simultaneously zero FP and zero FN in prompting and characterising CJD, our method of detection and quantification of basal ganglia intensity distributions proves to reach maximum specificity and sensitivity. We differentiate without ambiguity all CJD cases (sporadic and variant) from healthy controls and further characterise the CJD patients into two subgroups of human spongiform encephalopathies, sporadic and variant. More validation will be performed in future work, when more patient data are available.

The reader can refer to a more detailed version of this paper in [28].

VI. Conclusion

We presented a method for the detection of hypersignals in GM internal nuclei from multisequence MR images. The particular context of our application is that of human spongiform encephalopathies, prion protein diseases referred as CJD. The technique employs intensity and spatial normalization, noise removal with feature enhancement, foveal segmentation for the detection of hyperintensities, and *a priori* anatomical information for refined registration and removal of FPs. We are able to prompt 15/15 prion disease cases with no FPs or FNs.

Our method further allows the quantification of intensity distributions in basal ganglia, as we introduce two MRI-based ratios that differentiate between patients and normals, and between CJD forms. The caudate nuclei are highlighted as main areas of diagnosis of sCJD, in agreement with the histological data. In vCJD patients, we find higher hyperintensities in the pulvinar than in the other internal nuclei, which confirms the visually based radiological observations related to CJD.

Our method proves as reliable as the visual interpretation of radiologists for the detection of basal ganglia hypersignals. Moreover, it automatically yields quantitative data from MR patients with CJD, which could be used for patient follow-up and to evaluate the efficiency of therapeutic procedures. Our study demonstrates the value of MRI for a prospective noninvasive diagnosis of sCJD and the characterisation of prion diseases, as we clearly differentiate sporadic from variant CJD cases.

References

[1] R. D'Agostino and M. Stephens, *Goodness-of-Fit Techniques*. New York: Marcel Dekker, 1986.

[2] J. Ashburner and K. J. Friston, "Voxel-based morphometry—the methods," *NeuroImage*, vol. 11, pp. 805–821, 2000.

[3] M. M. Bahn, D. K. Kido, W. Lin, and A. L. Pearlman, "Brain magnetic resonance diffusion abnormalities in imaging in Creutzfeldt-Jakob disease," *Arch. Neurol.*, vol. 54, pp. 1411–1415, 1997.

[4] M. M. Bahn and P. Parchi, "Abnormal diffusion-weighted magnetic resonance images in Creutzfeldt-Jakob disease," *Arch. Neurol.*, vol. 56, pp. 577–583, 1999.

[5] J. P. Brandel, "Clinical aspects of human spongiform encephalopathies, with the exception of iatrogenic forms," *Biomed. Pharmacother*, vol. 53, pp. 14–18, 1999.

[6] J. P. Brandel, N. Delasnerie-Laupretre, J. L. Laplanche, J. J. Hauw, and A. Alpetrovitch, "Diagnosis of Creutzfeldt-Jakob disease: Effect of clinical criteria on incidence estimates," *Neuroradiol.*, vol. 54, pp. 1095–1099, 2000.

[7] P. Cachier, E. Bardinet, D. Dormont, X. Pennec, and N. Ayache, "Iconic feature-based nonrigid registration: The PASHA algorithm," *Comput. Vision Image Understand.*, vol. 89, no. 2–3, pp. 272–298, Feb. 2003.

[8] C. Chatfield, *Statistics for Technology: A Course in Applied Statistics*, 3rd ed. Norwell, MA: Chapman Hall, 1983.

[9] A. C. F. Colchester, S. A. Hojjat, R. G. Will, and D. Collie, "Quantitative validation of MR intensity abnormalities in variant CJD," *J. Neurol. Neurosurg. Psychiatry*, vol. 73, no. 2, p. 213, 2002.

[10] A. C. F. Colchester, S. A. Hojjat, I. Zerr, and D. A. Collie, "MR intensity analysis to discriminate variant, sporadic CJD, and non-CJD dementia patients," *J. Neurol. Neurosurge. Psychiatry*, vol. 75, p. 41, 2004.

[11] D. L. Collins, A. P. Zijdenbos, V. Kollokian, J. G. Sled, N. J. Kabani, C. J. Holmes, and A. C. Evans, "Design and construction of a realistic digital brain phantom," *IEEE Trans. Med. Imag.*, vol. 17, no. 3, pp. 463–468, Jun. 1998.

[12] A. Coulthard, K. Hall, P. T. English, P. G. Ince, D. J. Burn, and D. Bates, "Quantitative analysis of MRI signal intensity in new variant Creutzfeldt-Jakob disease," *Br. J. Radiol.*, vol. 72, pp. 742–748, 1999.

[13] J. A. de Priester, G. H. Jansen, J. R. de Kruijk, and J. T Wilmink, "New MRI findings in Creutzfeldt-Jakob disease: High signal in the globus pallidus on T1-weighted images," *Neuroradiology*, vol. 41, pp. 265–268, 1999.

[14] P. Demaerel, A. Baert, W. Vanopdensboch, and R. Robberecht, "Diffusion weighted magnetic resonance imaging in Creutzfeldt-Jakob disease: research letter," *Lancet*, vol. 349, pp. 847–848, 1997.

[15] D. Dormont, "New variant of Creutzfeldt-Jakob disease," *Eur. Surveil.*, vol. 5, no. 9, pp. 95–97, 2000.

[16] R. O. Duda, P. E. Hart, and D. H. Stork, *Pattern Classification*, 2nd ed. New York: Wiley, 2000.
[17] M. Finkenstaedt, A. Szudra, I. Zerr, S. Poser, J. Hise, J. Stoebner, and T. Wener, "MR imaging of Creutzfeldt-Jakob disease," *Radiology*, vol. 3, pp. 793–798, 1991.
[18] H. J Gertz, H. Henkes, and J. Cervos-Navarro, "Creutzfeldt-Jakob disease: correlation of MRI and neuropathologic findings," *Neurology*, vol. 38, no. 9, pp. 1481–1482, 1988.
[19] M. A. González Ballester, A. Zisserman, and M. Brady, "Estimation of the partial volume effect in MRI," *Med. Image Anal.*, vol. 6, no. 4, pp. 389–405, 2002.
[20] S. Haïk, J. P. Brandel, C. Oppenheim, V. Sazdovitch, J. J. Dormont, D. Hauw, and C. Marsault, "Sporadic CJD mimicking variant CJD with bilateral increased signal in the pulvinar," *Neurology*, vol. 58, pp. 148–149, 2002.
[21] S. Haïk, D. Dormont, B. A. Faucheux, C. Marsault, and J. J. Hauw, "Prion protein deposits in magnetic resonance imaging signal abnormalities in Creutzfeldt-Jakob disease," *Ann. Neurol.*, vol. 51, no. 6, pp. 797–799, 2002.
[22] A. Hojjat, D. Collie, and A. C. F. Colchester, "The putamen intensity gradient in CJD diagnosis," in *Medical Imaging and Computer Assisted Surgery (MICCAI 2002)*, T. Dohi and R. Kikinis, Eds. New York: Springer, 2002, vol. 2488, ser. Lecture Notes in Computer Science, pp. 524–531.
[23] J. P. Hornak, The basics of MRI. [Online]. Available: http://www.cis.rit.edu/htbooks/mri/
[24] E. W. Hsu and S. Mori, "Analytical expressions for the NMR apparent diffusion coefficients in an anisotropic system and a simplified method for determining fiber orientation," *Magn. Reson. Med.*, vol. 34, pp. 194–200, 1995.
[25] D. E. Job, S. Whalley, H. C. ad McConnell, M. Glabus, E. C. Johnstone, and S. M. Lawrie, "Structural gray matter differences between first-episode schizophrenics and normal controls using voxel-based morphometry," *Neuroimage*, vol. 17, pp. 880–889, 2002.
[26] G. B. Karas, E. J. Burton, S. A. R. B. Rombouts, R. A. van Schijndel, J. T. O'Brien, P. Scheltens, I. G. McKeith, D. Williams, C. Ballard, and F. Brakhof, "A comprehensive study of gray matter loss in patients with Alzheimer's disease using optimized voxel-based morphometry," *Neuroimage*, vol. 18, pp. 895–907, 2003.
[27] L. Lemieux, U. C. Wieshman, N. F. Moran, D. R. Fish, and S. D. Shorvon, "The detection and significance of subtle changes in mixed-signal brain lesions by serial MRI scan matching and spatial normalization," *Med. Image Anal.*, vol. 2, no. 3, pp. 227–242, 1998.
[28] M. G. Linguraru, M. A. González Ballester, E. Bardinet, D. Galanaud, S. Haïk, B. Faucheux, J. J. Hauw, P. Cozzone, D. Dormont, J. P. Brandel, and N. Ayache, Automated analysis of basal ganglia intensity distribution in multisequence MRI of the brain—Application to Creutzfeldt-Jakob disease INRIA, Le Chesnay, France, Res. Rep. RR-5276, 2004.
[29] M. G. Linguraru, M. A. González Ballester, and N. Ayache, "A multiscale feature detector for morphological analysis of the brain," in *Medical Image Computing and Computer-Assisted Intervention*, E. E. Randy and M. P. Terry, Eds. New York: Springer, 2003, vol. 2879, ser. Lectures Notes in Computer Science, pp. 738–745.
[30] M. G. Linguraru, M. Brady, and R. English, "Foveal algorithm for the detection of microcalcification clusters: A FROC analysis," in *Medical Image Computing and Computer-Assisted Intervention*, ser. Lecture Notes in Computer Science, C. Barillot, D. R. Haynor, and P. Hellier, Eds. New York: Springer, 2004, vol. 3217, pp. 813–820.
[31] M. G. Linguraru, "Feature detection in mammmographic image analysis," Ph.D. dissertation, Univ. Oxford, Oxford, U.K., 2002.
[32] J. C. Mazziotta, A. W. Toga, A. C. Evans, P. T. Fox, J. Lancaster, K. Zilles, R. P. Woods, T. Paus, G. Simpson, B. Pike, C. J. Holmes, D. L. Collins, P. M. Thompson, D. MacDonald, M. Iacoboni, T. Schormann, K. Amunts, N. Palomero-Gallagher, S. Geyer, L. Parsors, K. L. Narr, N. Kabani, G. Le Goualher, M. Boomsma, T. Cannon, R. Kawashima, and B. Mazoyer, "A probabilistic atlas and reference system for the human brain: International Consortium for Brain Mapping (ICBM)," *Philos. Trans. Roy. Soc. Lond. B, Biol. Sci.*, vol. 356, no. 1412, pp. 1293–1322, 2001.
[33] W. Milton, S. Atlas, E. Lavi, and J. Moliman, "Magnetic resonance imaging of Creutzfeldt-Jakob disease," *Ann. Neurol.*, vol. 29, pp. 438–440, 1991.
[34] P. Moon and D. E. Spencer, "The specification of foveal adaptation," *J. Opt. Soc. Amer.*, vol. 33, pp. 233–248, 1943.
[35] M. Onofrj, T. Fulgente, D. Gambi, and G. Macchi, "Early MRI findings in Creutzfeldt-Jakob disease," *J. Neurol.*, vol. 240, pp. 423–426, 1993.
[36] C. Oppenheim, J. P. Brandel, J. J. Hauw, J. P. Deslys, and B. Fontaine, "MRI and the second French case of vCJD," *Lancet*, vol. 356, pp. 253–254, 2000.
[37] S. Ourselin, A. Roche, S. Prima, and N. Ayache, "Block matching: A general framework to improve robustness of rigid registration of medical images," in *Third International Conference on Medical Robotics, Imaging and Computer Assisted Surgery (MICCAI 2000)*, A. M. DiGioia and S. Delp, Eds. New York: Springer, vol. 1935, ser. Lectures Notes in Computer Science, pp. 557–566.
[38] G. S. Pearl and R. E. Anderson, "Creutzfeldt-Jakob disease: high caudate signal on magnetic resonance imaging," *South. Med. J.*, vol. 82, pp. 1177–1180, 1989.
[39] A. H. Peden, M. W. Head, D. L. Ritchie, J. E. Bell, and J. W. Ironside, "Preclinical vCJD after blood transfusion in a *PRNP* codon 129 heterozygous patient," *Lancet*, vol. 364, pp. 527–529, 2004.
[40] D. Rueckert, A. Frangi, and J. A. Schnabel, "Automatic construction of 3D statistical deformation models of the brain using nonrigid registration," *IEEE Trans. Med. Imag.*, vol. 22, no. 8, pp. 1014–1025, Aug. 2003.
[41] A. Schroeter, I. Zerr, K. Henkel, and H. J. Tschampa, "Magnetic resonance imaging in the clinical diagnosis of Creutzfeldt-Jakob disease," *Arch. Neurol.*, vol. 57, pp. 1751–1757, 2000.
[42] J. Serra, *Image Analysis and Mathematical Morphology*. New York: Academic, 1982.
[43] S. Skare, "Optimisation strategies in diffusion tensor MR imaging," Ph.D. dissertation, Karolinska Univ., Stockholm,, Sweden, 2002.
[44] D. D. Stark, W. G. Bradley, and W. G. Bradley, Jr, *Magnetic Resonance Imaging*, 3rd ed. New York: Mosby, 1999.
[45] J. Talairach and P. Tournoux, *Co-Planar Stereotaxic Atlas of the Human Brain*. New York: Thieme, 1988.
[46] H. Urbach, J. Klisch, and H. K. Wolf *et al.*, "MRI in sporadic Creutzfeldt-Jakob disease: Correlation with clinical and neuropathological data," *Neuroradiology*, vol. 40, pp. 65–70, 1998.
[47] K. Van Leemput, "Quantitative analysis of signal abnormalities in MR imaging for multiple sclerosis and Creutzfeldt-Jakob disease," Ph.D. dissertation, Katholieke Universiteit Leuven, Leuven, The Netherlands, 2001.
[48] K. Van Leemput, F. Maes, D. Vandermeulen, A. Colchester, and P. Suetens, "Automated segmentation of multiple sclerosis lesions by model outlier detection," *IEEE Trans. Med. Imag.*, vol. 20, no. 8, pp. 677–688, Aug. 2001.
[49] J. Weickert, *Anisotropic Diffusion in Image Processing*, B. G. Teubner, Ed. Stuttgart, Germany: Teubner, 1998.
[50] C. F. Westin, S. E. Maier, B. Khidhir, P. Everett, F. A. Jolesz, and R. Kikinis, "Image processing for Diffusion Tensor Magnetic Resonance Imaging," in *Medical Imaging And Computer Assisted Surgery (MICCAI 1999)*. New York: Springer, 1999, ser. Lecture Notes in Computer Science, pp. 441–452.
[51] R. G. Will, M. Zeidler, G. E. Stewart, M. A. Macleod, J. W. Ironside, S. N. Cousens, J. Mackenzie, K. Estibeiro, A. J. E. Green, and R. S. G. Knight, "Diagnosis of new variant Creutzfeldt-Jakob disease," *Ann. Neurol.*, vol. 47, pp. 575–582, 2000.
[52] M. Zeidler, R. J. Sellar, D. A. Collie, R. S. G. Knight, G. E. Stewart, M. A. Macleod, J. W. Ironside, S. N. Cousens, A. F. C. Colcester, D. M. Hadley, and R. G. Will, "The pulvinar sign on magnetic resonance imaging in variant Creutzfeldt-Jakob disease," *Lancet*, vol. 355, pp. 1412–1418, 2000.
[53] I. G. Zubal, C. R. Harrell, E. O. Smith, Z. Rattner, G. Gindi, and P. B. Hoffer, "Computerized three-dimensional segmented human anatomy," *Med. Phys.*, vol. 21, pp. 299–302, 1994.